Supplementary Information

A new angle on dynamic depolarized light scattering: number-averaged size distribution of nanoparticles in focus

Christoph Geers [a], Laura Rodriguez-Lorenzo [a], Dominic Urban [a], Calum Kinnear [a,b,c], Alke Petri-Fink [a,b], Sandor Balog [a]*

[a] Adolphe Merkle Institute, University of Fribourg, Chemin des Verdiers 4, 1700 Fribourg, Switzerland

[b] Chemistry Department, University of Fribourg, Chemin du Musée 9, 1700 Fribourg, Switzerland

[c] Institute & School of Chemistry, The University of Melbourne, 30 Flemington Rd – 3010, Australia

Table of Content

Correlation function of depolarized scattering from polydisperse nanoparticles

We utilize that correlation is a linear operation, and the correlation function corresponding to a given particle size is weighted by the intensity of depolarized scattering. Accordingly, the intensity-weighted correlation function can be expressed as

$$(1) \qquad g_1(t) = \frac{\int_0^\infty P(r)\, I_{vh}(r)\, e^{-\Gamma(q,r)\, t}\, dr}{\int_0^\infty P(r)\, I_{vh}(r)\, dr}$$

where $P(r)$ describes the probability density distribution of the particle radii and $I_{vh}(r)$ is the intensity of depolarized scattering from a particle of radius r. The intensity of depolarized scattering can be expressed through the depolarization ratio ρ

$$(2) \qquad I_{vh} = \rho \times I_{vv}$$

defined as

$$(3) \qquad \rho \equiv \frac{I_{vh}}{I_{vv}}$$

where the subscripts v and h denote the vertical and horizontal polarizations with respect to the polarization of the laser. Both I_{vv} and ρ may be a function of particle size, wavelength of the laser, and angle of scattering.[1, 2]

First, we estimate the dependence of I_{vv} on the radius of gold particles via the Mie theory.[3, 4] The results show that the intensity of polarized scattering (I_{vv}) from a spherical gold particle of radius r is proportional to the square of the particle volume $V(r)$ (Figure S1a) - up to a radius of approximately 60 nm - and rather independent of the angle of scattering (Figure S1b). Figure S1c shows the scattering and absorption spectra of gold particles, and Figure S1d shows the dependence of the scattering and absorption coefficient at a given wavelength on the particle size. The results, obtained at the wavelength of our laser, show that for diameters below approx. 120 nm the gold particles may be treated as classical 'Rayleigh particles', that is the light absorption and scattering is proportional to V (particle volume) and V^2, respectively. Therefore, one can write

$$(4) \qquad I_{vv}(r, q) \propto V^2(r),$$

and the correlation function can be now written to involve the depolarization ratio

$$(5) \qquad g_1(t, q) = \frac{\int_0^\infty P(r)\, \rho(r)\, V^2(r)\, e^{-\Gamma(q,r)\, t}\, dr}{\int_0^\infty P(r)\, \rho(r)\, V^2(r)\, dr} = \frac{\int_0^\infty P(r)\, \rho(r)\, r^6\, e^{-\Gamma(q,r)\, t}\, dr}{\int_0^\infty P(r)\, \rho(r)\, r^6\, dr}.$$

The size limit that still preserves these relations is both material dependent and a function of the wavelength. In general, laser wavelengths being in the proximity of the peak of the localized surface plasmon resonance will decrease the upper size limit.

We determine next the depolarization ratio of gold NPs. For particles that are small compared to the wavelength of the incident light, the induced dipole moment is linearly proportional to the external electric field: [3]

$$(6) \qquad \mathbf{p} = \epsilon\, \bar{\alpha}\, \mathbf{E}$$

where ϵ is the absolute permittivity, $\mathbf{p} \equiv (p_x, p_y, p_z)$, $\mathbf{E} \equiv (e_x, e_y, e_z)$, and $\bar{\alpha}$ is the so-called polarizability tensor:

$$(7) \qquad \bar{\alpha} = \alpha_{ij} \equiv \begin{pmatrix} e_x p_x & e_x p_y & e_x p_z \\ e_y p_x & e_y p_y & e_y p_z \\ e_z p_x & e_z p_y & e_z p_z \end{pmatrix}.$$

For an axially symmetric NP (such as a spheroid with axes L_x, L_y, L_z), the orientation-averaged polarizability tensor is also symmetric and can be rewritten in a diagonal form:

$$(8) \qquad \bar{\alpha} \equiv \begin{pmatrix} \alpha_x & 0 & 0 \\ 0 & \alpha_y & 0 \\ 0 & 0 & \alpha_z \end{pmatrix}$$

where

$$(9) \qquad \alpha_i \equiv V \frac{\left(\frac{n_p}{n}\right)^2 - 1}{1 + G_i\left(\left(\frac{n_p}{n}\right)^2 - 1\right)},$$

and n_p and n are the refractive indices of the particle and the surrounding medium, respectively. G_i is a geometrical factor

$$(10) \qquad G_i \equiv \frac{L_x L_y L_z}{2} \int_0^\infty \frac{dq}{(L_i^2 + q)\sqrt{(L_x^2 + q)(L_y^2 + q)(L_z^2 + q)}}$$

that takes into account the axes of the particles.[3] $\sum_i^{x,y,z} G_i = 1$ and $0 < G_i \leq 1$, and for perfect spheres $G_x = G_y = G_z = 1/3$. For particles with shape anisotropy $G_i \neq G_j$, and thus $\alpha_i \neq \alpha_j$, which gives rise to depolarized scattering. The depolarization factor of randomly oriented (orientation-averaged) particles can be expressed as [5, 6]

$$(11) \qquad \rho = \frac{A - B}{3A + 2B}$$

where $A \equiv \sum_i^{x,y,z} |\alpha_i|^2$ and $B \equiv \mathrm{Re}\left[\sum_{i<j}^{x,y,z} \alpha_i^* \alpha_j\right]$. Both A and B being proportional to V^2 indicates that for a homogenous particle being small compared to the wavelength of the incident light, ρ is not an explicit function of overall particle size but only a function of the ratios of L_x, L_y, L_z, representing shape anisotropy. It is worthwhile to mention that while a non-zero ρ can originate from shape anisotropy of the particle, it can also result from internal anisotropy, e.g. from an internal crystalline structure. The intensity of depolarized scattering from a small spherical particle having a crystalline internal structure is also proportional to the square of the particle volume, and thus $I_{vh} \propto r^6$.[7] This finding was based on the argument that the intensity is proportional to the square of the optical anisotropy, which stems from the polycrystalline nature of the particles, and one assumes that the total volume occupied by the crystalline regions, i.e. the domains of atomic arrays within a particle, is proportional to the total volume.

a

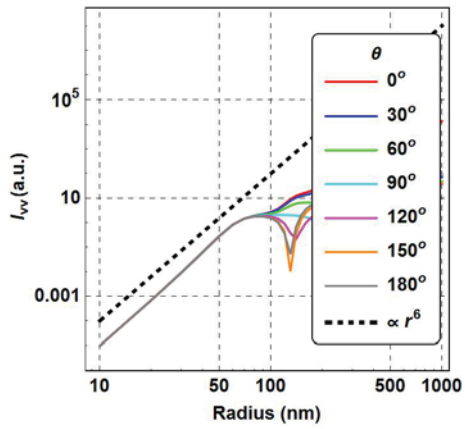

b

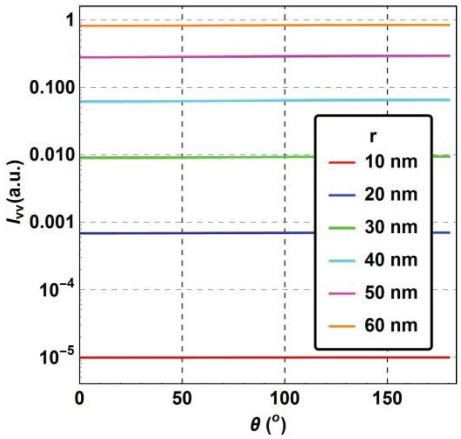

c

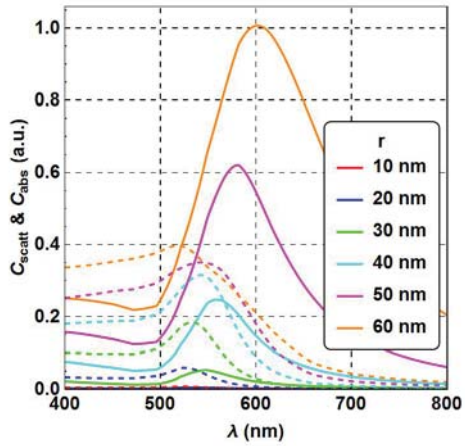

d

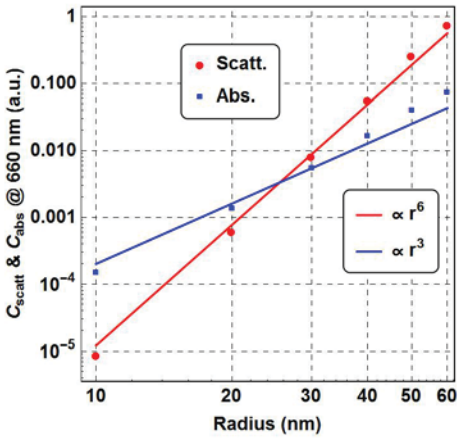

Figure S1: Results of Mie theory applied to describe light scattering and absorption from spherical gold particles suspended in water (n = 1.33) and illuminated with a plane wave of λ = 660 nm (n = 0.14 + i 3.7) at room temperature (22 °C). (a) I_{vv} as a function of particle radius for several scattering angles. (b) I_{vv} as a function of scattering angle for several particle radii. (c) Scattering (solid lines) and absorption (dashed lines) cross sections of gold particles of different radii as a function of wavelength. (d) Scattering and absorption cross section of gold particles at λ = 660 nm as a function of particle radius (full symbols). The solid lines indicate their dependence on particle radius. Since round gold nanoparticles do exhibit a certain degree of shape anisotropy (Figure 1) as well as internal anisotropy,[8] it can be expected that both contribute to depolarized scattering,[9] although the relative weight of their contribution is particle dependent. Additionally, ρ is a nontrivial function of the wavelength, for the refractive index is a function of the wavelength, and the refractive index is a function of particle size as well.[10] Nevertheless, the dependence of the latter is found to be rather moderate when the particle size is already beyond a few nm,[11] and beyond this regimeρ(r) becomes practically constant. This constant, ρ(r) ≅ ρ, can be brought in front of the integral and consequently will vanish:

(12) $$g_1(t,q) = \frac{\int_0^\infty P(r)\, r^6\, e^{-\Gamma(q,r)\, t}\, dr}{\int_0^\infty P(r)\, r^6\, dr}.$$

We expand the negative exponential into a power series about $t = 0$

(13) $$e^{-\left(\Gamma_T(q,r) + \Gamma_R(r)\right) t} = 1 - \frac{k_B T}{\pi \eta}\left(\frac{6}{8}\frac{1}{r^3} + \frac{q^2}{6}\frac{1}{r}\right) t + \left(\frac{k_B T}{\pi \eta}\right)^2 \left(\frac{9}{32}\frac{1}{r^6} + \frac{q^2}{8}\frac{1}{r^4} + \frac{q^4}{72}\frac{1}{r^2}\right) t^2 + \cdots,$$

and after substituting this series into Equation 12, we finally arrive at a correlation function that is expressed via the raw moments of the number-averaged particle size distribution

(14) $$g_1(t) = 1 - \frac{k_B T}{\pi \eta}\left(\frac{6}{8}\frac{\langle r^3\rangle}{\langle r^6\rangle} + \frac{q^2}{6}\frac{\langle r^5\rangle}{\langle r^6\rangle}\right) t + \left(\frac{k_B T}{\pi \eta}\right)^2 \left(\frac{9}{32}\frac{1}{\langle r^6\rangle} + \frac{q^2}{8}\frac{\langle r^2\rangle}{\langle r^6\rangle} + \frac{q^4}{72}\frac{\langle r^4\rangle}{\langle r^6\rangle}\right) t^2 + \cdots,$$

where

(15) $$\langle r^n\rangle \equiv \int_0^\infty P(r)\, r^n dr$$

is the n^{th} raw moment of $P(r)$.

Influence of polydispersity on DDLS spectra

At sufficiently short times, the decay of the correlation function is simply proportional to time

(16) $$g_1(t) \cong 1 - \langle\Gamma\rangle t.$$

Therefore, collecting dynamic light scattering spectra frequently consists of recording correlation functions at several angles, and afterwards quantifying and plotting the exponent $\langle\Gamma\rangle$ as a function of q^2. This is because the corresponding data points are expected to define a straight line whose intercept and slope are equal to $\langle 6D_R\rangle$ and $\langle D_T\rangle$, respectively. The influence of polydispersity on DDLS spectra can be already well grasped by analysing the behaviour of this linear relationship. The first moment is given by

(17) $$\langle\Gamma\rangle = \frac{k_B T}{\pi \eta}\left(\frac{6}{8}\frac{\langle r^3\rangle}{\langle r^6\rangle} + \frac{q^2}{6}\frac{\langle r^5\rangle}{\langle r^6\rangle}\right),$$

where $\langle D_R\rangle = \frac{k_B T}{\pi \eta}\frac{1}{8}\frac{\langle r^3\rangle}{\langle r^6\rangle}$ and $\langle D_T\rangle = \frac{k_B T}{\pi \eta}\frac{1}{6}\frac{\langle r^5\rangle}{\langle r^6\rangle}$. Already this term contains a unique feature: while translational diffusion is a function of the so-called Z-average: $\frac{\langle r^6\rangle}{\langle r^5\rangle}$, rotational diffusion is another function of two raw moments: $\sqrt[3]{\frac{\langle r^6\rangle}{\langle r^3\rangle}}$. These two values are equal only in the case of monodisperse particles, and both increase with polydispersity. Figure S5 demonstrates the influence of polydispersity on DDLS spectra. The results show $g_1(t)$ functions obtained from lognormal distributions of particle radius with different polydispersity indices. The correlation functions are characterized in terms of average relaxation rate $\langle\Gamma\rangle$ plotted as a function of q^2, where from both the evolution of the corresponding intercept $\langle 6D_R\rangle$ and slope $\langle D_T\rangle$ are obtained.

It is also worth considering the dispersion of Γ. Its value is usually defined by the coefficient of variation of $P(\Gamma)$:

(18) $$\delta\Gamma \equiv \frac{\sqrt{\langle\Gamma^2\rangle - \langle\Gamma\rangle^2}}{\langle\Gamma\rangle}.$$

$\delta\Gamma$ is a function of only σ, and is frequently determined by using the approach of cumulant expansion.[17, 18] We obtain that

(19) $$\langle\Gamma^2\rangle = 2\left(\frac{k_B T}{\pi\,\eta}\right)^2\left(\frac{9}{32}\frac{1}{\langle r^6\rangle}+\frac{q^2}{8}\frac{\langle r^2\rangle}{\langle r^6\rangle}+\frac{q^4}{72}\frac{\langle r^4\rangle}{\langle r^6\rangle}\right),$$

and δΓ can be evaluated by using the raw moments of the radius. Next we analyse the dependence of δΓ on the degree of size polydispersity. For comparison, δΓ corresponding uniquely to translational diffusion is also calculated. When DLS spectra are obtained from I_{vv} and depolarization is negligible, the terms resulting from rotational diffusion are not present. In this case δΓ(DLS) is calculated via $\langle\Gamma\rangle = \frac{k_B T}{\pi\,\eta}\frac{q^2}{6}\frac{\langle r^5\rangle}{\langle r^6\rangle}$ and $\langle\Gamma^2\rangle = 2\left(\frac{k_B T}{\pi\,\eta}\right)^2\frac{q^4}{72}\frac{\langle r^4\rangle}{\langle r^6\rangle}$. When $q\,r \ll 1$, which is usually the case at small scattering angles

(20) $$\delta\Gamma(\mathrm{DDLS}) \cong \sqrt{\frac{\langle r^6\rangle}{\langle r^3\rangle^2}-1}$$

and

(21) $$\delta\Gamma(\mathrm{DLS}) \cong \sqrt{\frac{\langle r^4\rangle\,\langle r^6\rangle}{\langle r^5\rangle^2}-1}.$$

For a lognormal distribution

(22) $$\delta\Gamma(\mathrm{DDLS}) \cong \sqrt{(1+\sigma^2)^9-1}$$

and

(23) $$\delta\Gamma(\mathrm{DLS}) \cong \sigma.$$

These relationships have two important consequences: First, compared to standard dynamic light scattering, depolarized scattering considerably enhances the 'apparent' polydispersity present in $g_1(t)$, for at low polydispersity $\delta\Gamma(\mathrm{DDLS}) \cong 3\sigma$, which is three times larger than δΓ(DLS). Therefore DDLS is able to resolve any narrow size distribution better than DLS. Second, δΓ(DDLS) rises above 100% when σ is beyond ~30%. Such high values of δΓ in DLS spectra are usually attributed to multimodality; however in the case of DDLS, it is an inherent property and not the signature of multimodality. The consequence is that in this regime a not 'heavy-tailed' unimodal distributions of P(Γ) is not be able to describe DDLS spectra.[8]

a

b

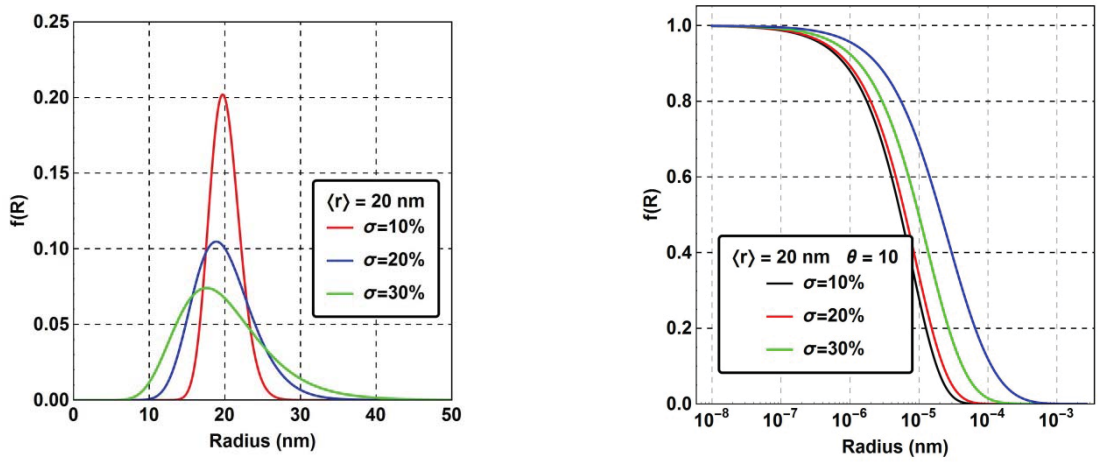

c

d

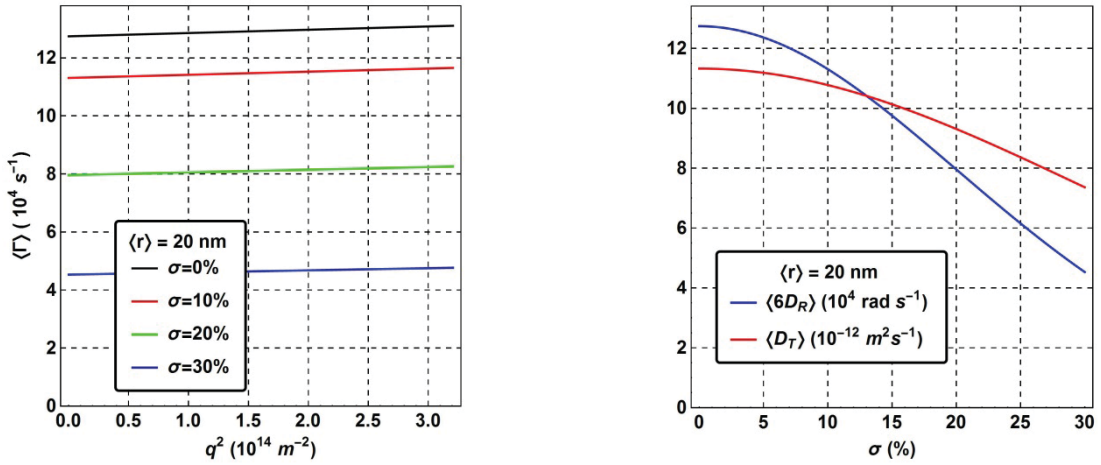

Figure S5. The influence of polydispersity on DDLS spectra of round particles. (a) Lognormal distribution of particle radius with different polydispersity indices. (b) The corresponding $g_1(t)$ functions. (c) The average relaxation rate $\langle\Gamma\rangle$ as a function of q^2. (d) Both the intercept $\langle 6D_R\rangle$ and slope $\langle D_T\rangle$ of the $\langle\Gamma\rangle$ vs. q^2 curve decreases with polydispersity.

The lognormal distribution

The lognormal distribution is described by two parameters: μ and ε

$$P(r) = \frac{1}{\sqrt{2\pi}\, r\, \varepsilon} e^{-\frac{(\ln r - \mu)^2}{2\varepsilon^2}}. \quad (24)$$

The average value is

$$\langle r\rangle = e^{\mu+\frac{\varepsilon^2}{2}}. \quad (25)$$

We express the degree of dispersion by the so-called polydispersity index: σ ≡ standard deviation divided by the mean, which by definition is equal to the coefficient of variation. It can be shown that

$$\sigma = e^{-\mu-\frac{\varepsilon^2}{2}}\sqrt{e^{2\mu+\varepsilon^2}(e^{\varepsilon^2}-1)}. \quad (26)$$

Expressing the lognormal distribution directly with $\langle r \rangle$ and σ, we obtain

$$(27) \qquad P(r) = \frac{1}{\sqrt{2\pi \ln(1+\sigma^2)}\, r}\, e^{-\frac{\left(\ln(1+\sigma^2) + 2\ln r - 2\ln\langle r\rangle\right)^2}{8\ln(1+\sigma^2)}}.$$

Then, the j^{th} raw moment of $P(r)$ can be written as a function of the average particle size and polydispersity index

$$(28) \qquad \langle r^j \rangle = \langle r \rangle^j (1+\sigma^2)^{\frac{1}{2}(j-1)j}.$$

Z-average

Z-average of polydisperse particles is always bigger than the number-averaged mean: $\langle r^6 \rangle / \langle r^5 \rangle > \langle r \rangle$. This can be understood by considering the fact that the raw moments can be also written as a function of the number-averaged mean and polydispersity index: $\langle r^j \rangle = \langle r \rangle^j \times f(n, \sigma)$. In the case of lognormal distribution: $\langle r^j \rangle = \langle r \rangle^j \times (1+\sigma^2)^{\frac{1}{2}(j-1)j}$. Since $\sigma^2 > 0$ and j is a positive integer, it follows that $\langle r^j \rangle > \langle r \rangle^j$. Similarly, it can be shown that $\langle r^{j+1} \rangle / \langle r^j \rangle = \langle r \rangle \times (1+\sigma^2)^j$, which means that $\langle r^{j+1} \rangle / \langle r^j \rangle > \langle r \rangle$.

TEM versus light scattering

Though standard TEM analysis is the first and basic tool when it comes to characterizing particles, it is not well-suited to determine hydrodynamic size because it is not an in situ approach.[12] Firstly, the presence of a thin citrate coating on the NPs,[13] invisible in TEM, will influence the hydrodynamics. But perhaps even more important and worth noting is that TEM may easily become user-biased, especially when thresholding methods are used to define the edges of the NPs. Second, while the raw moments $\langle \Gamma^n \rangle$ obtained by the polynomial functions and their relations to $\langle r^n \rangle$ are established by a model-independent approach, one deals with an ill-posed inverse problem, due to the character of the Laplace transform. Owing to the nature of such problems, modelling is frequently introduced. This step is usually based on complementary information collected independently. Although models are always incomplete, they are nonetheless able to account for certain selected characteristic features of the sample. The model we introduced here is that of the use of the lognormal distribution of spheres, whose shape captures rather well that of the distribution obtained from TEM. Additionally, the values estimated via a parametric statistical distribution depend on the analytical model itself, and there are many parametric statistical distributions that have been applied to describe particle systems.[14] Hence by using a different model, one should not expect to find exactly the same result. Third, one should not disregard that the 'modus operandi' of TEM and DDLS are rather different: The physical phenomena underpinning these two techniques and the related steps (i.e. the mathematical operations used for deriving secondary, tertiary, etc. variables starting from the primary data) are apart from one another, as in fact, they do not measure the same physical quantities at all. While they both measure certain distribution of random variables that are related to particle size distribution, the relationships between the different sets of variables and the particle size are actually different in both cases. While TEM image analysis is based on the geometrical interpretations of a two-dimensional 'footprint' of a three-dimensional particle projected onto a plane, the hydrodynamic size is inferred from

a random interference pattern whose temporal fluctuation relate to hydrodynamic diffusion phenomena. This also means that an uncertainty - here corresponding to the degree of polydispersity - propagates differently. This is because the given sets of the mathematical relationships used for determining particle size are not identical. For example using TEM, one may estimate the size via more than one way. This is because the particles are neither perfectly spherical nor uniform in shape; that is the deviations from the spherical shape are irregular and quite arbitrary, and thus, the shape itself is polydisperse too. In general, perimeter and area may be correlated or uncorrelated. Since the particles observed in TEM resemble to convex polygons with high degrees of central symmetry, the perimeter and area are correlated positively. Nevertheless, it matters whether one estimates perimeter- or area-equivalent size from the cross-sections projected onto the micrograph, for the propagation of uncertainty is not the same. For example, perimeter-equivalent diameter is estimated via P/π, while area-equivalent diameter is done via: $\sqrt{4A/\pi}$. The consequence is that the related size polydispersity indices are not equal: $\sigma(P) \equiv \frac{\sqrt{\langle r(P)^2\rangle - \langle r(P)\rangle^2}}{\langle r(P)\rangle} = \frac{\sqrt{\langle P^2\rangle - \langle P\rangle^2}}{\langle P\rangle}$ and $\sigma(A) \equiv \frac{\sqrt{\langle r(A)^2\rangle - \langle r(A)\rangle^2}}{\langle r(A)\rangle} = \frac{\sqrt{\langle A\rangle - \langle\sqrt{A}\rangle^2}}{\langle\sqrt{A}\rangle}$. It can be shown that $\sigma(P) \neq \sigma(A)$. Fourth, regarding dynamic light scattering, the hydrodynamic radius is also defined by means of an equivalent radius that represents a perfect sphere having the same diffusion coefficients. Beside overall size, hydrodynamic radius is also a function of shape. This has at least two consequences: a), two different particles of different size and shape may have identical hydrodynamic radius, and b), heterogeneity in shape will also contribute to the polydispersity of the hydrodynamic radius. To show this let us analyse the ideal case of regular spheroids. The two-dimensional projection of a spheroid is an ellipsoid, whose perimeter is $P \cong \pi\left(3(A+B) - \sqrt{(3A+B)(A+3B)}\right)$, where 2A and 2B are the major- and minor axes, respectively. The degree of elongation of an ellipsoid is usually described by the aspect ratio: $p \equiv A/B$. One can find infinite number of ellipsoids whose perimeter-equivalent radii are the same, but their aspect ratios are not equal. TEM analysis of perimeter-equivalent size distribution would classify these shapes as of equivalent size, except for their e.g. circularities and aspect ratios. The corresponding hydrodynamic radii would be calculated via the Perrin equations. The relaxation rates corresponding to a spheroid are (rotational: R, translational: T) [15, 16]:

$$\Gamma_R(A,p) = 6\frac{k_B T}{8\pi\eta}\frac{1}{A^3}\frac{3}{2}\frac{\left(2-\frac{1}{F(p)^2}\right)F(p)-1}{1-\frac{1}{p^4}}, \quad (29)$$

$$\Gamma_T(A,p,q) = q^2\frac{k_B T}{6\pi\eta}\frac{1}{A}F(p), \quad (30)$$

and

$$F(p) = \sqrt{\frac{1}{1-\frac{1}{p^2}}}\,\mathrm{Ln}\left[p\left(1+\sqrt{1-\frac{1}{p^2}}\right)\right] \quad p \geq 1, \quad (31)$$

where A is the half of the major axis and p is the aspect ratio. In the limit of $p \to 1$, one obtains the expressions corresponding to spherical particles with radius of A. The hydrodynamic radius can be obtained by solving this

equation: $\Gamma_R(A,p) + \Gamma_T(A,p,q) = \Gamma(q,r)$, where $\Gamma(q,r) = 6D_R + q^2D_T$. It is easy to show that at a constant perimeter, the higher the aspect ratio the smaller the hydrodynamic radius, even at moderate aspect ratios. Therefore, even if the perimeter-equivalent size is kept uniform, the corresponding hydrodynamic radius will not be uniform. Consequently, in the case of not perfectly spherical particles when the perimeter exhibits dispersion, it may be expected that the dispersion of the hydrodynamic size exceeds that of the perimeter-equivalent size. The shape of the gold particles presented here are overall not far from that of a sphere. Their shape, however, are not regular but arbitrary. Regardless, since the relaxation rate corresponding to rotational diffusion shows an enhanced sensitivity towards the relative changes in the hydrodynamic size,[8] it can be expected that the overall relationship between shape heterogeneity and dispersion in the hydrodynamic radius is formally analogous, and thus a very similar tendency is preserved.

Nanoparticle tracking analysis

Nanoparticle tracking analysis was performed at room temperature (25 °C), using a digital microscope system (NS500, NanoSight, Malvern Instruments, λ =488 nm, P max. < 60 mW). To observe and track approximately 50 particles within the microscope's field of view, the particle suspension was diluted to a concentration of 10^8-10^9 particles mL^{-1}. Laser scattering from the NPs was visualized in the microscope (NA=0.4), and the scattering centers undergoing Brownian motion were imaged by a CMOS detector. With a frame rate of 25 frames per second, shutter speed of 25 ms, and a camera gain of 400, five videos of 90 s length were recorded and subsequently analyzed by the NTA 3.0 software with detection thresholds settings equal to 8-9. From the videos of the visualized scattering centers, the particle traces were constructed and the mean-square displacement $\langle x^2 + y^2 \rangle$ in two dimensions was calculated as a function of time. The diffusion coefficient (D) and hydrodynamic radius are quantified via: $\langle x^2(t) + y^2(t) \rangle = 4\,D\,t$ and $r = \frac{k_B\,T}{6\,\pi\,h}\frac{1}{D}$.

The instrument was unable to track the small NPs (Au1 NPs) with the performance available. Considering the characterization of the Au2 NPs (50 nm), tracking and analysis determined larger particles (mean: 81 nm, polydispersity index: 62%) and a wider distribution, but the overall tendency is not entirely inconsistent when compared to TEM and DDLS (Figure S2). This is likely due to the fact that while NTA is fairly reliable for large particles, its sensitivity to NPs at the lowest end of the accessible size range is cut off (below ~30nm in case of Au NPs). The cause is, among others, the limited dynamic range and sensitivity of the camera, and therefore, one obtains a size distribution that is skewed towards larger sizes.[17]

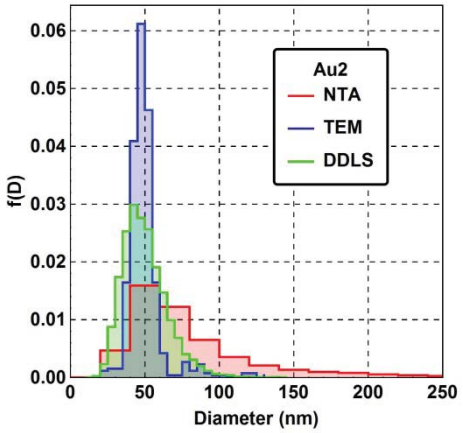

Figure S2. Number-averaged size distributions obtained by using NTA, TEM (perimeter-equivalent diameter), and DDLS (lognormal model).

Taylor-Aris dispersion

The initial concentration profile (t=0) was located within a small region at the injection point (x = 0), and the observation time was greater than the time required for the particles to diffuse radially across the capillary, that is, $\frac{x}{v} > 1.4\,Y^2$. The optical extinction observed as a function of time at position x (taylogram) has the following form [18-20]

$$(32) \qquad C(t,r) \propto \sqrt{\frac{x}{t\,V}}\,\exp\left(-\frac{v^2\left(t-\frac{x}{v}\right)^2}{4\,t\left(D_T+\frac{Y^2v^2}{48\,D_T}\right)}\right)$$

where x is the distance between detection and injection points, v mean flow velocity, Y capillary radius, and $D_T = D_T(r)$ translational diffusion coefficient of the particles of hydrodynamic radius r. By considering the size-dependent optical extinction $\mu(r)$ of the AuNPs at the detection wavelength, Equation 24 can be extended for polydisperse particles:

$$(33) \qquad C(t) \propto \frac{\int_0^\infty P(r)\,\mu(r)C(t,r)\,dr}{\int_0^\infty P(r)\mu(r)dr}.$$

In the case of Au NPs, absorption dominates at the used wavelength (Figure S3), and thus:

$$(34) \qquad C(t) \propto \frac{\int_0^\infty P(r)\,r^3\,C(t,r)\,dr}{\int_0^\infty P(r)\,r^3\,dr}.$$

Therefore, taylograms were simulated via Equation 26 by using the number-averaged size distribution of the hydrodynamic radius obtained from DDLS without involving other free or adjustable parameters. The simulations are compared with experimental TDA spectra on Figure S4.

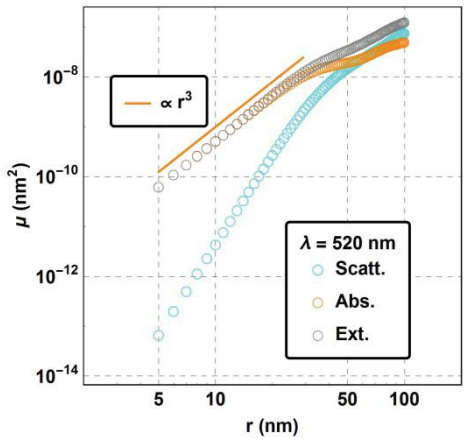

Figure S3. The dependence of the extinction, scattering and absorption coefficients on the radius of Au NPs at λ = 520 nm, calculated via the Mie theory.[3, 4]

a

b

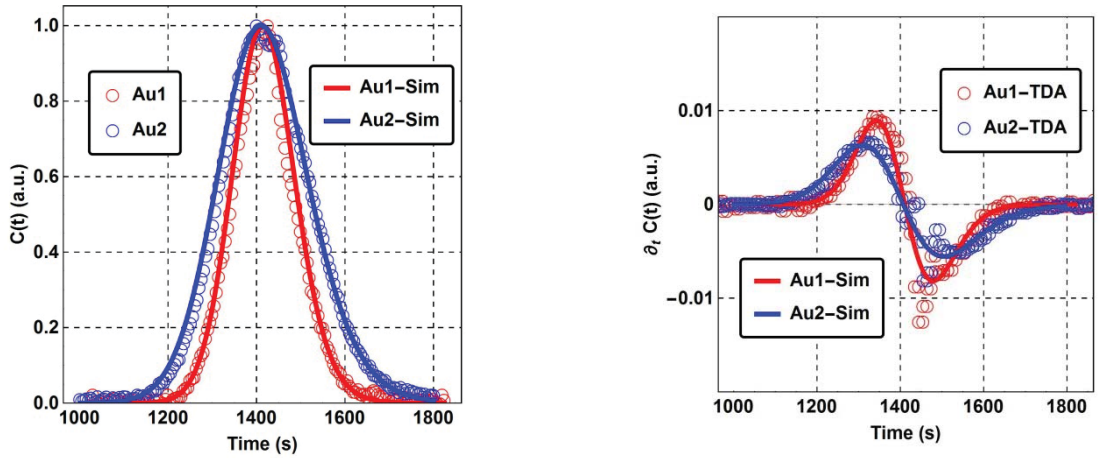

Figure S4. a) Experimental taylograms (symbol) and simulation (solid line) corresponding to the Au1 and Au2 NPs. TDA detection window was at 85 cm. b) The first time derivatives of experimentally recorded taylograms $\partial_t C(t)$ and simulations. The experimental data were averaged over a time interval of 10s for improving the signal-to noise-ratio.

The simulations from DDLS and the experimental TDA spectra are in very good qualitative agreement. Before comparing the values of hydrodynamic size determined from DDLS and TDA, the apparent size probed by TDA must be calculated in the case of polydisperse samples. After sufficiently long time, the shape of a taylogram corresponding to uniform particles is essentially a Gaussian

$$C(t, r) \sim e^{-\frac{\left(t-\frac{x}{v}\right)^2}{2\sigma^2}}, \quad (35)$$

whose width is proportional to the degree of dispersion and hence contains the information relating to hydrodynamic radius. Starting from Equation 24, it can be shown that:

(36) $$\sigma^2(r,t) = \left(\frac{2\,D_T}{v^2} + \frac{Y^2}{24\,D_T}\right)t = \left(\frac{1}{3v^2}\frac{k_B T}{\pi\,\eta}\frac{1}{r} + \frac{\pi\,Y^2\,\eta}{4\,k_B T}r\right)\,t.$$

In the case of polydispersity, each particle - weighted by its absorption coefficient - contribute to the width of the taylogram. Thus, the apparent particle size is determined from:

(37) $$\langle\sigma^2(t)\rangle = \frac{\int_0^\infty P(r)\,r^3\sigma^2(r,t)\,dr}{\langle r^3\rangle},$$

and the width of the taylogram is the function of the raw moments of the number-averaged size distribution of the hydrodynamic radius:

(38) $$\langle\sigma^2(t)\rangle = \left(\frac{1}{3v^2}\frac{k_B T}{\pi\,\eta}\frac{\langle r^2\rangle}{\langle r^3\rangle}\right)t + \left(\frac{\pi\,Y^2\eta}{4\,k_B T}\,\frac{\langle r^4\rangle}{\langle r^3\rangle}\right)t.$$

The second term dominates the right side of Equation (38), that is,

(39) $$\langle\sigma^2(t)\rangle \cong \left(\frac{\pi\,Y^2\eta}{4\,k_B T}\,\frac{\langle r^4\rangle}{\langle r^3\rangle}\right)t.$$

Therefore, by fitting the taylogram one essentially determines $\langle r^4\rangle/\langle r^3\rangle$. In the case of lognormal distribution

(40) $$\langle r^4\rangle/\langle r^3\rangle = \mu(1+\sigma^2)^3.$$

Depolarized scattering from multimodal suspensions

Let the particle radius be r, and the mass-based concentration (e.g. μg/mL) of the particle suspension be C. Then, the total mass of NPs in a volume V is

(41) $$m = C\,V,$$

and the total number of uniform particles is

(42) $$n = \frac{m}{\delta\frac{4}{3}\pi\,r^3},$$

where δ is the mass density of the particles. In case of polydisperse spherical particles, Equation 41 can be written as

(43) $$C\,V\; = \;\sum_{i=1}^{n} m_i = \delta\sum_{i=1}^{n} V_i = \delta\frac{4}{3}\pi\sum_{i=1}^{n} r_i^3,$$

where n is the total number of polydisperse particles, m_i the mass, V_i the volume, and r_i the radius of the i^{th} particle. The term $\sum_{i=1}^{n} r_i^3$ can be written as $n\frac{1}{n}\sum_{i=1}^{n} r_i^3$. By definition, this is the third raw moment of the particle size distribution

(44) $$\langle r^3\rangle \equiv \frac{1}{n}\sum_{i=1}^{n} r_i^3,$$

and hence,

(45) $$n = \frac{V\,C}{\delta\frac{4}{3}\pi\langle r^3\rangle}.$$

For a multimodal suspension with k modes:

$$(46) \qquad m = \sum_{j=1}^{k} m_j = \sum_{j=1}^{k} C_j V_j$$

where V_j and C_j are respectively the total volume and mass-based concentration of the j^{th} particle mode of the suspension. The total number of particles within a given mode is

$$(47) \qquad n_j = \frac{C_j V_j}{\delta \frac{4}{3}\pi \langle r_j{}^3 \rangle}.$$

The corresponding average intensity of depolarized scattering is

$$(48) \qquad \langle I_j \rangle = \sum_{h=1}^{n_j} \rho_{j,h}\, r_{j,h}{}^6 = n_j \langle \rho_j\, r_j{}^6 \rangle.$$

When the depolarization ratio is independent of the particle size: $\langle \rho_j\, r_j{}^6 \rangle = \langle \rho_j \rangle \langle r_j{}^6 \rangle$. The correlation function of a multimodal suspension having k modes thus can be expressed by the intensity-weighted sum of the respective modes:

$$(49) \qquad g_1(t,q) = \frac{\sum_{j=1}^{k} \langle I_j \rangle\, g_{1,j}(t)}{\sum_{j=1}^{k} \langle I_j \rangle} = \sum_{j=1}^{k} A_j\, g_{1,j}(t),$$

where $A_j \equiv \frac{\langle I_j \rangle}{\sum_{j=1}^{k} \langle I_j \rangle}$. Therefore, in the case of bimodal suspensions the relaxation rate is the intensity-weighted sum of the relaxation rates of the respective modes:

$$(50) \qquad \langle \Gamma \rangle = A_1 \frac{k_B T}{\pi \eta} \left(\frac{6}{8} \frac{\langle r_1{}^3 \rangle}{\langle r_1{}^6 \rangle} + \frac{q^2}{6} \frac{\langle r_1{}^5 \rangle}{\langle r_1{}^6 \rangle} \right) + A_2 \frac{k_B T}{\pi \eta} \left(\frac{6}{8} \frac{\langle r_2{}^3 \rangle}{\langle r_2{}^6 \rangle} + \frac{q^2}{6} \frac{\langle r_2{}^5 \rangle}{\langle r_2{}^6 \rangle} \right).$$

Since $A_j < 1$, the value of $\langle \Gamma \rangle$ is between the relaxation rates of the respective modes, i.e. $\langle \Gamma_1 \rangle \leq \langle \Gamma \rangle \leq \langle \Gamma_2 \rangle$ when $\langle \Gamma_1 \rangle < \langle \Gamma_2 \rangle$.

Small-angle X-ray scattering and TEM of PEG-coated Au NPs

The SAXS spectrum of PEG-coated gold citrate nanoparticles (PEG-CH3 Au NPs) was interpreted by the following model:

$$(51) \qquad I(q) = \frac{\int_0^\infty P(r)\, V(r)^2\, \phi(q,r)^2 dr}{\int_0^\infty P(r)\, V(r)^2\, dr},$$

where P(r) describes the probability density function of the radius of the core, $V(r) = \frac{4}{3}\pi\, r^3$ is the volume and $\phi(q,r)^2 = \left\{ \frac{3}{(q\, r)^3} [\sin(q\, r) - q\, r\, \cos(q\, r)] \right\}^2$ is the form factor of a spherical particle of radius r. By definition, $\phi(q,r)^2$ is obtained via the three-dimensional Fourier transform of the spatial distribution of the electron density within the particle of radius r. For a homogeneous solid sphere of perfect central symmetry, the electron density is constant, and the form factor may be calculated via the three-dimensional Hankel transform:

$$(52) \qquad \phi(q,r)^2 = \left\{ \frac{1}{V(r)} \int_0^r 4\pi\, \frac{\sin qr'}{qr'} r'^2 dr' \right\}^2.$$

a

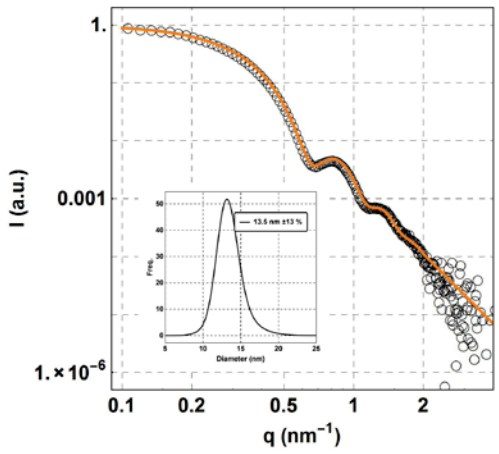

b

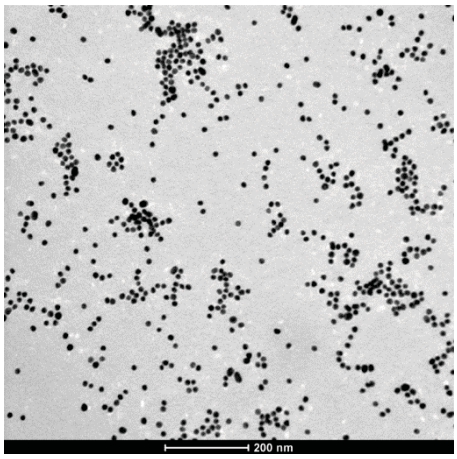

Figure S6. SAXS spectrum (a) and TEM micrograph (b) of the PEG-CH_3 Au NPs in aqueous phosphate buffer. SAXS: the best fit of the scattering intensity (solid line). The inset shows the obtained frequency distribution of the core diameter. TEM characterization of the core of these NPs determined 16.0 ± 2.6 nm (mean $\pm$ std). This is in good agreement with SAXS, and the small difference between the results (1.25 nm in radius) is attributed to the fact that particles are aspherical.

Correlation function of depolarized scattering from polymer-coated particles

In the presence of a polymer grafted or adsorbed onto the surface, the hydrodynamic radius may be expressed as a function of the core radius: $r_H = \gamma(r) \times r$, where $\gamma(r) > 1$ is a function that embodies properties related to the polymer, such as molecular weight, graft density, and conformation. Both conformation as well as surface coverage is affected by particle size. In the case of e.g. gold particles grafted with PEG, it has been reported that grafting density decreases with increasing core size, since a smaller particle allows an increased grafting density on the account of a higher surface curvature.[21, 22] The polymer shell may affect the depolarization ratio as well, for the LSPR is sensitive to changes in the local dielectric environment.[23] Nevertheless, the depolarization ratio is expected to remain practically constant over the particle size distribution. In the presence of a polymer shell $\langle r^n \rangle \rightarrow \langle {r_H}^n \rangle = \langle (\gamma(r) \times r)^n \rangle$, and it can be shown that

$$(53) \qquad g_1(t) = 1 - \frac{k_B T}{\pi \eta}\left(\frac{6}{8}\frac{\langle(\gamma(r)\times r)^3\rangle}{\langle(\gamma(r)\times r)^6\rangle} + \frac{q^2}{6}\frac{\langle(\gamma(r)\times r)^5\rangle}{\langle(\gamma(r)\times r)^6\rangle} \right) t + \cdots,$$

where

$$(54) \qquad \langle(\gamma(r) \times r)^n\rangle \equiv \int_0^\infty P(r)\,(\gamma(r) \times r)^n dr.$$

We expect that $\gamma(r)$ is a strictly monotonic function of r, and for particles with moderate polydispersity $\gamma(r)$ is practically constant over the size distribution: $\gamma(r) \cong \gamma$. Then: $\langle(\gamma(r) \times r)^n\rangle = \gamma^n \langle r^n \rangle$ and

(55) $$\frac{\langle(\gamma(r)\times r)^n\rangle}{\langle(\gamma(r)\times r)^m\rangle} = \frac{\langle r^n\rangle}{\gamma^{m-n}\langle r^m\rangle}.$$

Finally, we obtain:

(56) $$g_1(t) = 1 - \frac{k_B T}{\pi\eta}\left(\frac{6}{8}\frac{\langle r^3\rangle}{\gamma^3\langle r^6\rangle} + \frac{q^2}{6}\frac{\langle r^5\rangle}{\gamma\langle r^6\rangle}\right)t + \left(\frac{k_B T}{\pi\eta}\right)^2\left(\frac{9}{32}\frac{1}{\langle r^6\rangle} + \frac{q^2}{8}\frac{\langle r^2\rangle}{\gamma^4\langle r^6\rangle} + \frac{q^4}{72}\frac{\langle r^4\rangle}{\gamma^2\langle r^6\rangle}\right)t^2 + \cdots,$$

where γ represents the factor quantifying the hydrodynamic radius of the polymer shell.

Raw moments of P(Γ)

The field correlation function from polydisperse samples is frequently expressed as the Laplace transform of the probability density function describing the dispersion in the relaxation rate:[24, 25]

(57) $$g_1(t) = \int_0^\infty P(\Gamma)e^{-\Gamma t}\,d\Gamma = \sum_{j=0}^{\infty}\frac{1}{j!}\langle\Gamma^j\rangle t^j = 1 - \langle\Gamma\rangle t + \frac{1}{2}\langle\Gamma^2\rangle t^2 - \frac{1}{6}\langle\Gamma^3\rangle t^3 + \cdots.$$

Using the lognormal model, $\langle\Gamma\rangle$, $\langle\Gamma^{-2}\rangle$, and $\langle\Gamma^{-3}\rangle$ can be expressed as functions of $\langle r_H{}^n\rangle$:

(58) $$\langle\Gamma\rangle = \frac{k_B T}{\pi\eta}\left(\frac{1}{\gamma^3}\frac{3}{4(1+\sigma^2)^{12}\langle r\rangle^3} + \frac{1}{\gamma}\frac{q^2}{6(1+\sigma^2)^5\langle r\rangle}\right)$$

(59) $$\langle\Gamma^2\rangle = 2\left(\frac{k_B T}{\pi\eta}\right)^2\left(\frac{1}{\gamma^6}\frac{9}{32(1+\sigma^2)^{15}\langle r\rangle^6} + \frac{1}{\gamma^4}\frac{q^2}{8(1+\sigma^2)^{14}\langle r\rangle^4} + \frac{1}{\gamma^2}\frac{q^4}{6(1+\sigma^2)^9\langle r\rangle^2}\right)$$

(60) $$\langle\Gamma^3\rangle = 6\left(\frac{k_B T}{\pi\eta}\right)^3\left(\frac{1}{\gamma^9}\frac{9}{128(1+\sigma^2)^{36}\langle r\rangle^9} + \frac{1}{\gamma^7}\frac{3q^2}{64(1+\sigma^2)^{21}\langle r\rangle^7} + \frac{1}{\gamma^5}\frac{q^4}{95(1+\sigma^2)^{10}\langle r\rangle^5} + \frac{1}{\gamma^3}\frac{q^6}{1296(1+\sigma^2)^3\langle r\rangle^3}\right).$$

UV-Vis spectra of gold citrate nanoparticles incubated in BSA solution

a b

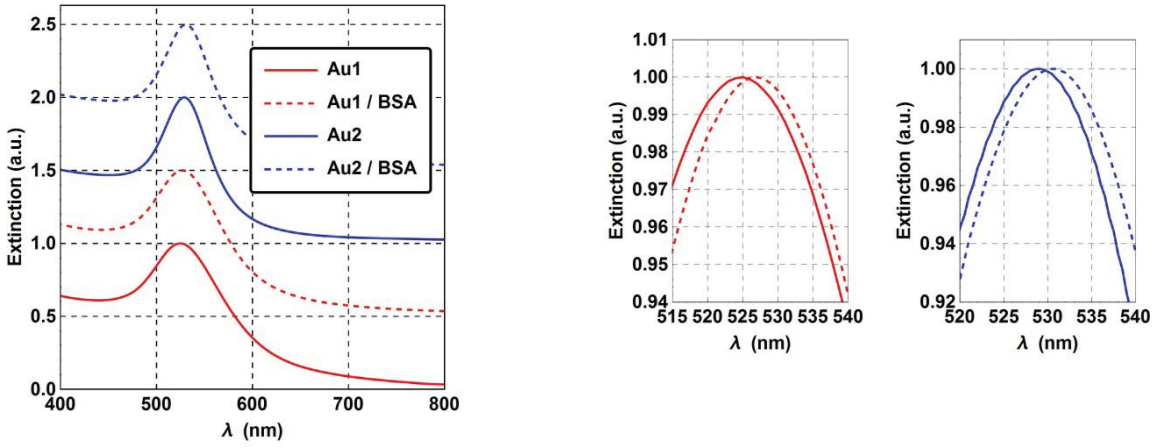

Figure S7. a) UV-Vis spectra of Au1 and Au2 NPs with and without the presence of BSA. The spectra are displaced vertically for the sake of visibility. b) Close-up view of the shift in the center of the LSPRs (Au1: from 525 nm to 527 nm, Au2: from 529 nm to 531 nm). The amplitudes are normalized.

Light scattering from nanoparticles in biological media

Light scattering is an ensemble technique and simultaneously probes billions of scattering centres, including those found in biological and physiological media. In particular, proteins abundantly found in cell culture media contribute significantly to polarized scattering (DLS).[26] However, compared to optically anisotropic NPs, the magnitude of

depolarized scattering (DDLS) from cell culture media is very small, which ensures an excellent selectivity towards the particles.[26] To demonstrate the advantage of DDLS over standard DLS, we measured scattering from silver nanoparticles (PVP-coated Ag NPs, Figure S8). The Ag NPs were synthesized as described by Andrade et al.[27] Briefly, Ag NPs stabilized with β-Cyclodextrin (β-CD) were prepared by adding 20 mL of an aqueous AgNO3 (0.01 M) solution at a 1 drop/s rate to a vigorously stirred, heated (60°C) solution containing 15 mL aqueous glucose (0.013 M), 15 mL aqueous NaOH (0.01 M) and 30 mL aqueous β-CD (0.015 M). Then, the suspension was dialyzed with deionized water to remove excess reactants. Subsequently, the Ag NPs were coated with polyvinylpyrrolidone Mw 8000 ([PVP] = 4 molecules per nm^2) to promote colloidal stability in biological media.

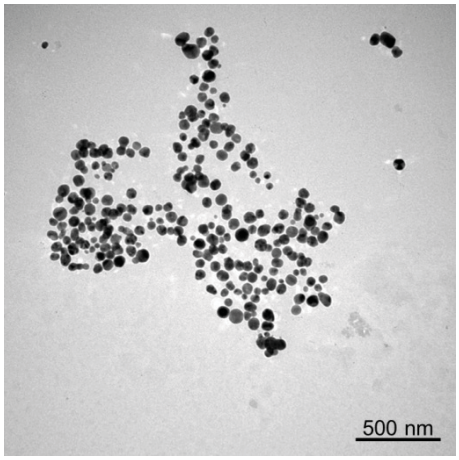

Figure S8. TEM micrograph of the PVP-coated Ag NPs.

The Ag NPs were suspended in water and then in cell culture medium (Roswell Park Memorial Institute (RPMI) supplemented with vol. 10% Fetal Bovine Serum (FBS) at 25 °C for 1 h. The visual appearance and the UV-Vis spectra of the samples are shown in Figure S9a and b. It is evident that at low particle concentration the media dominates both the visual appearance (#5) and the features of the UV-Vis spectra.

a b

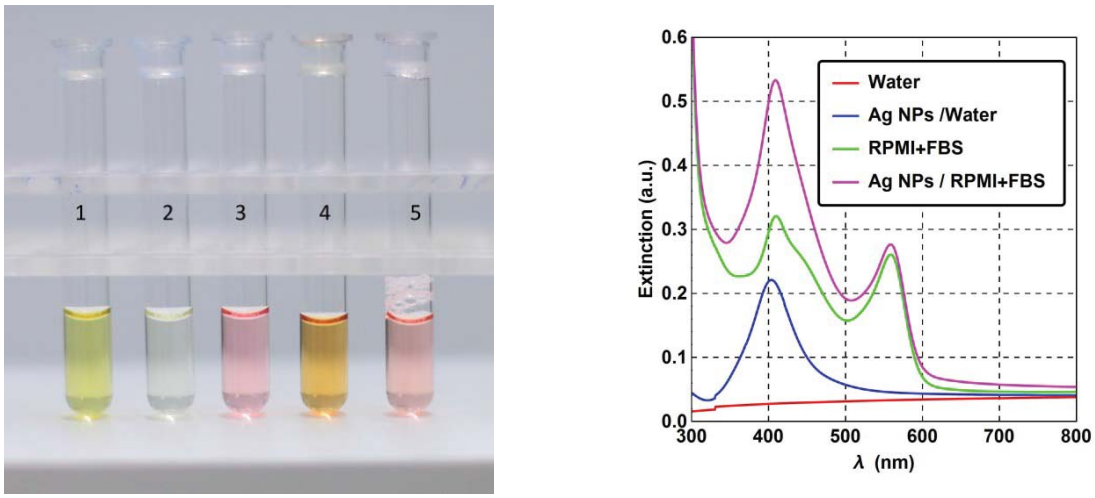

Figure S9. a) Photograph of the Ag NPs in water at 50 and 5 μg/mL concentrations (1 and 2), supplemented RPMI (3), and Ag NPs in RPMI+FBS at 50 and 5 μg/mL concentrations (4 and 5). b) UV-Vis spectra of the Ag NPs in water (5 μg/mL) and in supplemented RPMI.

Next we compared the corresponding scattering intensities and correlation functions. Figure S10 shows that compared to the Ag NPs, the magnitude of the depolarized scattering (I_{vh}) from the cell culture media is less than 1%. However, the magnitude of the polarized scattering (I_{vv}) from the cell culture media is over 50%, which may have crucial consequences on the analysis of the correlation function and the ability of determining particle size.

a b

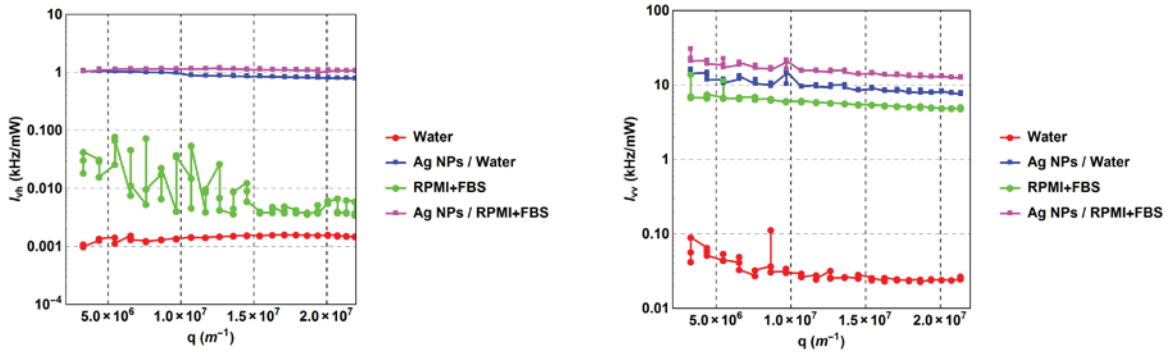

Figure S10. a) Depolarized scattering corresponding to DDLS (I_{vh}), and b) polarized scattering corresponding to standard DLS (I_{vv}).

This can be easily understood when one considers that the intensity auto-correlation function $g_2(t)$ is constructed via the following operation:

(61) $g_2(t) \equiv \frac{1}{\langle I\rangle^2}\frac{1}{T}\int_0^T I(t')\cdot I(t'+t)\,dt'$

where the angular bracket denotes averaging over time

(62) $\langle I\rangle \equiv \frac{1}{T}\int_0^T I(t)\,dt$

and I(t) is the intensity trace recorded over a time period of T. If the scattered field is Gaussian, the Siegert relation connects the intensity auto-correlation function with the field auto-correlation function:

(63) $g_2(t) = 1 + \beta|g_1(t)|^2.$

When one observes the fluctuations of a single coherent area (only one speckle) $\beta = 1$. Since it is only $g_2(t)$ that is accessible through experiments, the field auto-correlation function is derived via

(64) $g_1(t) = \sqrt{g_2(t) - 1}.$

where

(65) $g_2(t) - 1 = \frac{\langle I(t')\cdot I(t'+t)\rangle - \langle I\rangle^2}{\langle I\rangle^2}.$

For a dilute suspension of uniform NPs, the field correlation function is expected to be a negative exponential as a function of time

(66) $g_1(t) = e^{-\Gamma t}.$

In the presence of scattering from the constituents of the cell culture medium, the intensity trace can be decomposed into at least two terms:

(67) $I(t) = I_{NP}(t) + I_x(t).$

The first one corresponds to the NPs of interest, and the second one corresponds to the cell culture medium. It follows that $\langle I\rangle = \langle I_{NP}\rangle + \langle I_x\rangle$. Accordingly, $\langle I\rangle^2 = \langle I_{NP}\rangle^2 + 2\langle I_{NP}\rangle\langle I_X\rangle + \langle I_x\rangle^2$, and the intensity auto-correlation function will be composed of several terms:

(68) $g_2(t) - 1 = \frac{1}{\langle I\rangle^2}\langle\big(I_{NP}(t') + I_x(t')\big)\cdot\big(I_{NP}(t'+t) + I_x(t'+t)\big)\rangle - \frac{\langle I\rangle^2}{\langle I\rangle^2} =$

$$= \frac{\langle I_{NP}(t')\cdot I_{NP}(t'+t)\rangle}{\langle I\rangle^2} + \frac{\langle I_{NP}(t')\cdot I_x(t'+t)\rangle}{\langle I\rangle^2} + \frac{\langle I_x(t')\cdot I_{NP}(t'+t)\rangle}{\langle I\rangle^2} + \frac{\langle I_x(t')\cdot I_x(t'+t)\rangle}{\langle I\rangle^2} - \frac{\langle I_{NP}\rangle^2 + 2\langle I_{NP}\rangle\langle I_x\rangle + \langle I_x\rangle^2}{\langle I\rangle^2}.$$

The second and third terms are equivalent: $\langle I_{NP}(t')\cdot I_x(t'+t)\rangle = \langle I_x(t')\cdot I_{NP}(t'+t)\rangle$,

and thus

(69) $g_2(t) - 1 = \frac{\langle I_{NP}(t')\cdot I_{NP}(t'+t)\rangle - \langle I_{NP}\rangle^2}{\langle I\rangle^2} + 2\frac{\langle I_{NP}(t')\cdot I_x(t'+t)\rangle - \langle I_{NP}\rangle\langle I_x\rangle}{\langle I\rangle^2} + \frac{\langle I_x(t')\cdot I_x(t'+t)\rangle - \langle I_x\rangle^2}{\langle I\rangle^2}.$

If $I_{NP}(t)$ and $I_x(t)$ are statistically independent:

(70) $\langle I_{NP}(t')\cdot I_x(t'+t)\rangle = \langle I_{NP}(t')\rangle\langle I_x(t'+t)\rangle,$

and

(71) $2\frac{\langle I_{NP}(t')\cdot I_x(t'+t)\rangle - \langle I_{NP}\rangle\langle I_x\rangle}{\langle I\rangle^2} = 0.$

Consequently, in the presence of cell culture medium, the intensity auto-correlation function of DLS will be composed of at least two terms: one corresponds to the NPs of interest and the other does to the cell culture medium:

(72) $$g_2(t) - 1 = \frac{\langle I_{NP}(t') \cdot I_{NP}(t'+t) \rangle - \langle I_{NP} \rangle^2}{\langle I \rangle^2} + \frac{\langle I_x(t') \cdot I_x(t'+t) \rangle - \langle I_x \rangle^2}{\langle I \rangle^2}.$$

Indeed, Figure S11 clearly shows the presence of the media in the experimentally obtained DLS spectrum. While the scattering spectrum of Ag NPs in water exhibits two decays - a characteristic 'bimodal' feature of the DLS spectra of plasmonic NPs -, in cell culture media the scattering contribution further adds to the complexity of the decay and shape of the correlation function. Given that particle size is estimated via $g_2(t) - 1$, this influences the apparent size and may come with difficulties when interpreting real particle size. If the cellular medium is inert towards the suspended particles, or the interactions between NPs and the cellular media is moderate, one might be able to overcome this difficulty by characterizing a) the cellular media without NPs, b) the NPs in an aqueous 'empty' background', and finally c) the NPs in the fluid. However, cellular media are rarely inert towards NPs and induces several complex and simultaneous phenomena, such as protein adsorption, particle dissolution and aggregation.[28] In such cases this approach cannot be followed because the scattering 'reference' from the cellular media and NPs both become invalid.[29]

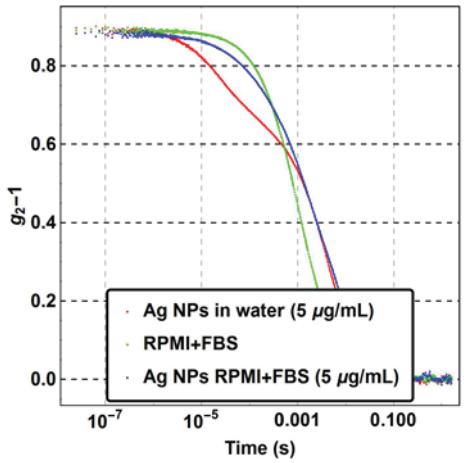

Figure S11: DLS intensity auto-correlation functions constructed from I_{vv} at $\theta = 20^o$.

References

1. B. Khlebtsov, V. Khanadeev and N. Khlebtsov, *Physical Chemistry Chemical Physics*, 2010, **12**, 3210-3218.
2. N. G. Khlebtsov, A. G. Mel'nikov, V. A. Bogatyrev, A. V. Alekseeva and B. N. Khlebtsov, *Opt Spectrosc.*, 2006, **100**, 448-455.
3. M. Quinten, *Optical Properties of Nanoparticle Systems: Mie and beyond*, Wiley-VCH Verlag GmbH, 2011
4. P. Laven, *Appl. Opt.*, 2003, **42**, 436-444.
5. N. G. Khlebtsov, A. G. Melnikov, V. A. Bogatyrev, L. A. Dykman, A. V. Alekseeva, L. A. Trachuk and B. N. Khlebtsov, *The Journal of Physical Chemistry B*, 2005, **109**, 13578-13584.
6. H. C. v. d. Hulst, *Light scattering by small particles*, Dover Publications, New York, 1981.
7. V. Degiorgio, R. Piazza and T. Bellini, *Advances in Colloid and Interface Science*, 1994, **48**, 61-91.
8. S. Balog, L. Rodriguez-Lorenzo, C. A. Monnier, B. Michen, M. Obiols-Rabasa, L. Casal-Dujat, B. Rothen-Rutishauser, A. Petri-Fink and P. Schurtenberger, *The Journal of Physical Chemistry C*, 2014, **118**, 17968-17974.

9. A. H. R. Koch, G. Lévêque, S. Harms, K. Jaskiewicz, M. Bernhardt, A. Henkel, C. Sönnichsen, K. Landfester and G. Fytas, *Nano Letters*, 2014, **14**, 4138-4144.
10. B. S. Lucía and O. T. Jorge, *Nanotechnology*, 2006, **17**, 1309.
11. L. B. Scaffardi, N. Pellegri, O. d. Sanctis and J. O. Tocho, *Nanotechnology*, 2005, **16**, 158.
12. B. Michen, C. Geers, D. Vanhecke, C. Endes, B. Rothen-Rutishauser, S. Balog and A. Petri-Fink, *Scientific reports*, 2015, **5**, 9793.
13. J.-W. Park and J. S. Shumaker-Parry, *Journal of the American Chemical Society*, 2014, **136**, 1907-1921.
14. H. G. Merkus, *Particle Size Measurement: Fundamentals, Practice, Quality*, Springer, 2009.
15. F. Perrin, *J. Phys. Radium*, 1934, **5**, 497-511.
16. F. Perrin, *J. Phys. Radium*, 1936, **7**, 1-11.
17. V. Filipe, A. Hawe and W. Jiskoot, *Pharm Res*, 2010, **27**, 796-810.
18. G. Taylor, *Proceedings of the Royal Society of London A: Mathematical, Physical and Engineering Sciences*, 1953, **219**, 186-203.
19. G. Taylor, *Proceedings of the Royal Society of London A: Mathematical, Physical and Engineering Sciences*, 1954, **225**, 473-477.
20. R. Aris, *Proceedings of the Royal Society of London A: Mathematical, Physical and Engineering Sciences*, 1956, **235**, 67-77.
21. P. D. Jadzinsky, G. Calero, C. J. Ackerson, D. A. Bushnell and R. D. Kornberg, *Science*, 2007, **318**, 430-433.
22. G. Zhang, Z. Yang, W. Lu, R. Zhang, Q. Huang, M. Tian, L. Li, D. Liang and C. Li, *Biomaterials*, 2009, **30**, 1928-1936.
23. K. L. Kelly, E. Coronado, L. L. Zhao and G. C. Schatz, *The Journal of Physical Chemistry B*, 2002, **107**, 668-677.
24. D. E. Koppel, *The Journal of Chemical Physics*, 1972, **57**, 4814-4820.
25. B. J. Frisken, *Appl. Opt.*, 2001, **40**, 4087-4091.
26. S. Balog, L. Rodriguez-Lorenzo, C. A. Monnier, M. Obiols-Rabasa, B. Rothen-Rutishauser, P. Schurtenberger and A. S. Fink, *Nanoscale*, 2015.
27. P. F. Andrade, A. F. de Faria, D. S. da Silva, J. A. Bonacin and M. d. C. Gonçalves, *Colloids and Surfaces B: Biointerfaces*, 2014, **118**, 289-297.
28. T. L. Moore, L. Rodriguez-Lorenzo, V. Hirsch, S. Balog, D. Urban, C. Jud, B. Rothen-Rutishauser, M. Lattuada and A. Petri-Fink, *Chemical Society Reviews*, 2015.
29. D. A. Urban, L. Rodriguez-Lorenzo, S. Balog, C. Kinnear, B. Rothen-Rutishauser and A. Petri-Fink, *Colloids and Surfaces B: Biointerfaces*, 2015.